

Volumetric velocimetry for small seeding tracers in large volumes

Yisheng Zhang Simon L. Ribergård Haim Abitan
Clara M. Velte

December 6, 2021

Abstract

This paper presents the volumetric velocity measurement method of small seeding tracer with diameter $5\ \mu\text{m} \sim 100\ \mu\text{m}$ for volume $\geq 500\ \text{cm}^3$. The size of seeding tracer is between helium-filled soap bubbles (HFSB) and di-ethyl-hexyl-sebacic acid ester (DEHS) droplets. The targeted measurement volume dimension equal to the volume of HFSB seeding, which will give a higher resolution of turbulence study. The relations between particle size, imaging and light intensity are formulated. The estimation of the imaging result are computed for the setup design. Finally, the methodology is demonstrated for turbulence velocity measurements in the jet flow, in which the velocities of averaged diameter $15\ \mu\text{m}$ air filled soap bubbles are measured in the volume of $\geq 2000\ \text{cm}^3$ and $\geq 9000\ \text{cm}^3$.

1 Introduction

It is still a problem in the research of turbulent flows for obtaining all the eddies from the largest primary size to a micron size in inertial sub-range. The main conflicts come from the tracer size, camera resolution and the intensity of light signal. There is a strong push for large volumetric velocity measurement using small tracers[1]. Normally, due to light scattering and characteristics length scale considerations, big tracers are used for tracing large eddies in big volumes, and smaller tracers are applied for micro-scale eddies in smaller volumes. As can be expected from Figure 1, there is a noticeable gap between attainable volumetric domains for large ($\geq 300\ \text{cm}^3$) and small ($1\ \mu\text{m} \sim 20\ \mu\text{m}$) tracers in the range between $10^4\ \text{cm}^3 \sim 10^4\ \text{cm}^3$.

As part of a long-term combined theoretical and experimental initiative, we are setting out to experimentally test the degree of locality of the interactions between wavenumber components [2]. This requires measurements that cover the ‘global’ dynamics of the flow, while also capturing as wide a bandwidth of the turbulent (temporal and spatial) spectrum as possible. Tracers of diameter $\sim 15\ \mu\text{m}$ with reasonable Stokes number can follow the flow accurately to the degree of spatio-temporal resolution in the experimental design while at the same time they are highly resilient and long-lived and therefore the most viable option from a practical point of view. Therefore, these smaller seeding particles are the key factor to these experiments.

Discetti and Coletti[5] summarized methods that have been developed to measure the full volumetric velocity (3D–3C, i.e. three-dimensional and three-component). In the past two decades, volumetric velocimetry has evolved from experiments at moderate scale of $10\ \text{cm}^3$ up to large scales of $10^4\ \text{cm}^3$ by various application experiments. The initial tomo-PIV experiment done by Elsinga et al. [4] was conducted with $1\ \mu\text{m}$ droplets in a volume of $13\ \text{cm}^3$. Later the larger

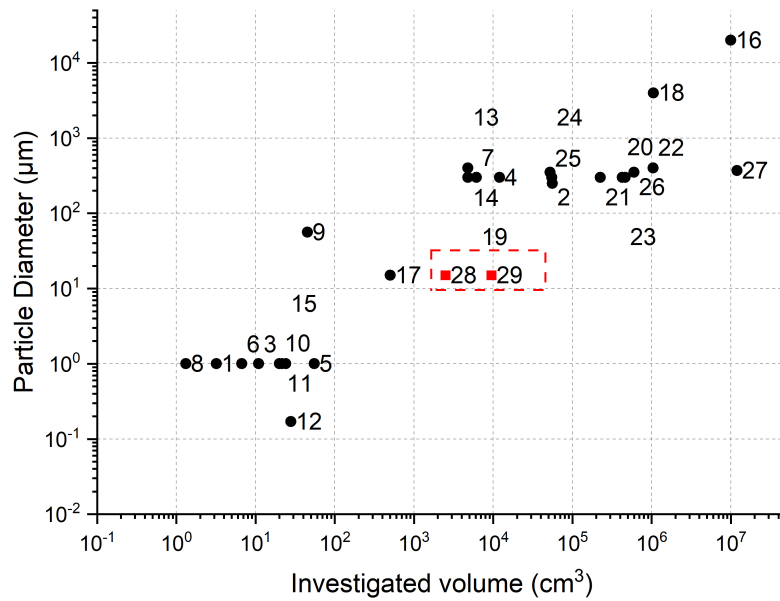


Figure 1: Compilation of volumetric velocimetry investigations in air flows: the particle diameter and the imaged volume. The labeled points refers to the researches in the references: 1, Atkinson et al.[14]; 2, Kühn et al.[15]; 3, Cafiero et al.[21]; 4, Caridi et al.[22]; 5, Boushaki et al.[23]; 6, Pröbsting et al.[24]; 7, Schneiders et al.[25]; 8, Schneiders et al.[26]; 9, Schneiders et al.[26]; 10, Elsinga et al.[4]; 11, Schröder et al.[27]; 12, Humble et al.[8]; 13, Terra et al.[28]; 14, Scarano et al.[6]; 15, Michaelis et al.[3]; 16, Hou et al.[29]; 17, Barros et al.[1]; 18, Bosbach et al.[30]; 19, Schneiders et al.[31]; 20, Huhn et al.[32]; 21, Schanz et al.[33]; 22, Bosbach et al.[34]; 23, Schanz et al.[35]; 24, Schanz et al.[36]; 25, Wolf et al.[37]; 26, Novara et al.[38]; 27, Schröder et al.[41]. The red squares 28 and 29 are the current study and the red area is the interested study area.

measurement volumes were obtained by volumetric velocimetry in air conducted by Schröder et al.[7], Humble et al.[8], Violato et al. [9] and Ghaemi and Scarano [10] Schröder et al. [11] and Atkinson et al. [14], which did not exceed 10^2 cm^3 measurement volume with micron-scale seeding tracers.

The main factors limiting the upscale of PIV to macroscopic dimensions are the limited illumination energy from the illumination source, the scattering efficiency of the tracers, the small optical aperture (due to large depth of field), and the sensitivity and spatial resolution of the camera sensors[6]. With low repetition rate(prolonging the exposure time) and millimeter scale Helium-filled Soap Bubbles(increasing scattering efficiency), larger measurement volumes can be observed to characterize large scale flow structure [15, 42].

For turbulence flows, the inherent instability and three dimensions requires high resolution time-resolved volumetric velocimetry. It is impossible to utilize millimeter scale tracers to measure the same scale turbulent structure, because the length scale of the structure is smaller than the tracer diameter, and the cut-off diameter of the particles deduced from cut-off frequency could be micron-scale[16]. The current investigation aims at characterizing both the 'global' flow structure and millimeter scale structure with micron-scale tracers.

With the capabilities of low resolution camera, the only option to capture the turbulence structure is to observe small tracers in a small measurement volume. Now with the development of camera sensor techniques, the high resolution cameras in recent years provide the possibility of capturing the intermediate-size turbulence structure in a larger volume, in which the whole evolution process of the turbulent spectrum can be observed. However, there is still a problem between the visibility of seeding tracers and the following effect of intermediate-size turbulence structure. In order to visualize small structures in the turbulence flow, micron-scale tracers are needed to follow the unstable and three dimensional millimetre scale structures. And as the result of reducing the tracer dimension, the signal from seeding tracers to camera would drop in quadratic proportion. For the purpose of solving this problem, this paper thus details the computation of particle image size with tracers, lens and camera parameters. Then with the desired turbulent scales, the relation among camera, light source and measurement volume is formulated to make sure that the particle images cannot travel across pixels (to avoid streaky particle images). Two examples of approximate $15 \mu\text{m}$ particles in a $> 2000 \text{ cm}^3$ volume and a $> 9000 \text{ cm}^3$ volume, that are 10 times larger than [1], are demonstrated at an acquisition frequency of $\sim 2 \text{ kHz}$. The current work thus documents how to design a time-resolved volumetric velocimetry experiment in a manner that the gap of smaller seeding particles for the target turbulent microscale structure in big volume for 'global' flow is filled. The paper is organized as follows. In the Section 2, the methodology that related from flow characteristics, seeding, illumination and imaging was formulated. To demonstrate the computation, a jet flow example was computed in Section 3, where we use the all the formulas in Section 2. The setup and experiment result corresponding to the computation in Section 3 was provided in Section 4. Finally, our conclusion and perspectives were given.

2 Methodology

2.1 Flow characteristics

The target smallest structure in the flow is characterized with length-scale ℓ and characteristic velocity $u(\ell)$. The timescale of these structure is [43]

$$\tau(\ell) \equiv \frac{\ell}{u(\ell)}. \quad (2.1)$$

Based on the timescale, the interested frequency is

$$f_i = \frac{1}{\tau(\ell)}. \quad (2.2)$$

According to the Shannon's sampling theorem, the camera minimum repetition rate f_c should be more than twice of the interested frequency $f_c \geq 2f_i$. Both the spatial resolution and the camera repetition are based on the flow length-scale and timescale.

2.2 Seeding

There are six factors that affects the particles to follow the flow[16, 44, 45]. Response time and Stokes number are related to the fidelity of tracer particles accurately following the flow[45]. Response time (τ_t) represents the characteristic time required for a tracer particle to reach an equilibrium condition after a flow disturbance. The response time is commonly calculated using the following form

$$\tau_t = d_p^2 \frac{\rho_p}{18\nu} \quad (2.3)$$

where d_p is the particle diameter, ρ_p is the particle density and ν is the kinematic viscosity of the ambient fluid. The Stokes number (Sk) is defined as the ratio of the characteristic time of a particle to a characteristic time of the interested flow (τ_f),

$$Sk = \frac{\tau_t}{\tau_f} \quad (2.4)$$

As the smallest eddies are characterized the timescale $\tau(\ell)$, the flow characteristic time equals to the timescale $\tau_f = \tau(\ell)$. In general, a Stokes number of 0.1 or less could return an acceptable flow tracing accuracy with errors below 1% [46].

In dynamic conditions like turbulent flows studied by Mei[16], the particle frequency response function H_p that is defined as the sinusoidal response of particle to a sinusoidal oscillation of the flow relates to the bias between the particle velocity and flow velocity,

$$\hat{v}(\omega) = H_p(\omega)\hat{u}(\omega), \quad (2.5)$$

where $\hat{v}(\omega)$ is the particle velocity amplitude at frequency ω , and $\hat{u}(\omega)$ is the flow velocity amplitude, both of which are deduced from particle oscillation function $v(t) = \hat{v}(\omega)e^{-i\omega t}$ and flow oscillation function $u(t) = \hat{u}(\omega)e^{-i\omega t}$.

Defining Stokes number in frequency domain ε with the frequency variable ω [16],

$$\varepsilon = \sqrt{\frac{\omega d_p^2}{2\nu}} \quad (2.6)$$

the energy transfer function deduced from the particle frequency response function is

$$|H_p(\omega)| = |H_p(\varepsilon)| = \frac{(1 + \varepsilon)^2 + (\varepsilon + \frac{2}{3}\varepsilon^2)^4}{(1 + \varepsilon)^2 + [\varepsilon + \frac{2}{3}\varepsilon^2 + \frac{4}{9}(\rho - 1)\varepsilon^2]^2}. \quad (2.7)$$

where, ρ is the density ratio of particles and ambient flow $\rho = \rho_p/\rho_f$, and ρ_f is the density of the ambient flow.

In Mei's study [16], the cut-off frequencies of the particles are based the 50% and 200% energy response, which means that $0.5 < |H_p(\omega)|^2 < 2$ implies very good response of the seeding particles. So the cut-off frequencies f_{cutoff} , the cut-off Stokes number ε_{cutoff} and the cut-off particle diameter d_{cutoff} can be computed from the follow equations:

$$\left\{ \begin{array}{l} \varepsilon_{cutoff} = \{\varepsilon : |H_p(\omega)|^2 \in \{0.5, 2\}\} \\ \varepsilon_{cutoff} \approx [2.380^{0.93} + (\frac{0.659}{0.561-\rho} - 1.175)^{0.93}]^{\frac{1}{0.93}}, \rho < 0.561 \\ \varepsilon_{cutoff} \approx [(\frac{3}{2\rho^{1/2}})^{1.05} + (\frac{0.932}{\rho-1.621})^{1.05}]^{\frac{1}{1.05}}, \rho > 1.621 \\ f_{cutoff} \approx \frac{\nu}{\pi} \left(\frac{\varepsilon_{cutoff}}{d_p}\right)^2 \\ d_{cutoff} \approx \varepsilon_{cutoff} \sqrt{\frac{\pi f_{cutoff}}{\nu}} \end{array} \right. \quad (2.8)$$

However, in practice the computation process is the reversed version: (1)find the particle parameter like diameter d_p and density ρ_p ; (2)compute the density ratio ρ and Stokes frequency domain number ε ; (3)get the energy transfer function result $|H_p(\omega)|^2$ and decide if the seeding type is suitable for the flow; (4)compute the cut-off frequency f_{cutoff} to see if it can cover the interested frequency range. To emphasis the unit of the parameters in the equation, kinematic viscosity in the equation (2.8) and (2.6) is expressed in terms of cm^2/s , and the diameter of particles is in the term of μm .

2.3 Imaging

The observed volume $V = L \times H \times W$ is imaged by cameras with the fixed optical magnification based on the sensor size. Define the pixel resolution l_s , pixel pitch Δ_{pix} , and aperture number f_s , the optical magnification of the imaging system can be deduced from the ratio of the focal lens to the working distance.

$$M = \frac{l_s \Delta_{pix}}{L} = \frac{d_i}{d_o} \quad (2.9)$$

where d_o is the distance from the object geometrical center to the lens center, d_i the distance from the image geometrical center to the lens center. The particle image τ_p on camera sensor can be computed from:

$$\tau_p = \frac{\sqrt{d_{op}^2 + d_s^2 + d_f^2}}{\Delta_{pix}} \quad (2.10)$$

where $d_{op} = Md_p$ is the particle diameter; d_s is diffraction limit spot diameter, which can be computed with aperture stop number f_s and light wave length λ

by $d_s = 2.44(1 + M)f_s\lambda$, d_f is the blur circle diameter. The depth of focus (DOF) δ_z is

$$\delta_z = 2d_s f_s \frac{1 + M}{M^2} = 4.88 f_s^2 \lambda \frac{(1 + M)^2}{M^2} \quad (2.11)$$

The diameter of the effective aperture D_a is

$$D_a = \frac{f}{f_s} \quad (2.12)$$

And the focal length f can satisfy the basic lens equation:

$$\frac{1}{f} = \frac{1}{d_o} + \frac{1}{d_i} \quad (2.13)$$

2.4 Scattered Light

In the PIV experiment, part of the incident light is imaged by the tracers onto the camera sensors. It is the scattered light that releases the information of the tracers. The light scattering properties of a homogeneous and isotropic sphere in a plane wave, which leads to the Lorenz-Mie Theory, are well documented in the literature (van de Hulst1981[47], Bohren and Huffmann1983[48], Mishchenko etc.2002 [49], Born and Wolf 1984[50]), thus only related final results are presented to obtain the light source budget.

The first step is to project the incident wave vector onto the scattering plane. From camera lens, the received electric field vector can be expressed as

$$\mathbf{E}_r = \frac{e^{-i\mathbf{k}_\omega \mathbf{r}_p}}{\mathbf{k}_\omega \mathbf{r}_p} \mathbf{M}_\beta \mathbf{M}_S \mathbf{M}_\varphi \mathbf{E}_0 \quad (2.14)$$

where \mathbf{E}_0 is incident plane wave vector, \mathbf{k}_ω is the incident wave vector, and \mathbf{r}_p is the scattering vector between the particle center and lens center, the angle between \mathbf{k}_ω and \mathbf{r}_p is ϑ , the scattering plane lies at an angle of φ , \mathbf{M}_S is the scattering matrix with sum of scattering functions, \mathbf{M}_β , and \mathbf{M}_φ is plan transform matrix (details to see Albrecht et al.[?] pages 79-126).

One dimensionless parameter defined as Mie parameters is important to the scattering intensity,

$$x_M = \frac{\pi d_p}{\lambda}. \quad (2.15)$$

For particles with Mie parameter $x_M > 10$, the scattered intensity increases with the second power of the particle diameter, which means geometrical optics can be applied for approximate computation. For the Lorenz-Mie region with $1 \leq x_M \leq 10$, the scattered intensity exhibits strong oscillations. The received light intensity is

$$I_r(\lambda, r, \vartheta) = \frac{c\epsilon}{2} |\mathbf{E}_r|^2 \quad (2.16)$$

where ϵ is the permittivity of the medium, c is the light speed.

The photons signal I_c received by the cameras are the inner product of the light intensity distribution function and the camera sensor quantum efficiency function $\Phi_{qe}(\lambda)$,

$$I_c = \int \int \Phi_{qe}(\lambda) I_r(\lambda, r, \vartheta) d\lambda dA. \quad (2.17)$$

The integral of the area depends on the aperture diameter. If the distance between particle and lens is much larger than the efficient aperture $r \gg D$ and the scattering angle is in the range of geometrical optics, the scattering angle can be considered as constant. Thus the integral is only the constant intensity multiplied by the efficient aperture area.

The signal-to-noise ratio SNR in this paper follows the definition of Scharnowski and Kahler[20], which used standard deviations of the image intensity and the noise:

$$SNR = \frac{\sigma_A}{\sigma_n}, \quad (2.18)$$

where σ_n is the standard deviation of the noise level, and σ_A is the standard deviation of the signal level, which can be approximated with number particle images per pixel N_{ppp} ,

$$\sigma_A = \frac{I_0}{2} \sqrt{N_{ppp} \cdot \left(\frac{\pi}{4} \tau_p^2 - 1 \right)} \quad (2.19)$$

The loss-of-correlation due to image noise F_σ is defined as,

$$F_\sigma = \frac{\sigma_A^2}{\sigma_A^2 + \sigma_n^2} = \left(1 + \frac{1}{SNR^2} \right)^{-1}. \quad (2.20)$$

Before experiments start, the noise level σ_n can be estimated from the camera manuals. From the theory analysis and experimental evaluation in [20], the loss-of-correlation F_σ increase strongly from 0.4 to 0.8 with linearly increment of light power. So the main focus of the light design is to pursue the higher F_σ below 0.8 under the limited light source budget.

2.5 Computation process

With all the knowledge in this section, the computation process can be summarized in the following sequence:

1. Compute the camera repetition rate from the timescale of the interested flows in equation (2.1) and (2.2).
2. Get the camera resolution by the ratio of smallest eddies to largest eddies, and select a camera satisfying the repetition rate and resolution.
3. Obtain the magnification M from equation (2.9).
4. Set the camera position according to the distance d_o computed from equation (2.9).
5. Define the cut-off frequency from the reciprocal of the timescale, estimate the particle diameter scale with $\varepsilon_{cutoff} = 0.1$, then compute the cut-off Stokes number ε_{cutoff} and the energy transfer function $|H_p(\omega)|^2$ with different types of seeding in the same range. Set the biggest seeding type with considering the energy loss and the cost.
6. Obtain the aperture stop number f_s from depth of field of the interested volume and the diffraction limit spot diameter d_s equation, and Obtain the focal length f from the d_o and M , compute and the seeding particle image diameter τ_p .

7. Take LEDs as the first consideration in the cases of large volumes [45], acquire the LEDs intensity chart, and compute the Mie-parameter x_M .
8. Design the light scattering angle as large as possible, the illumination distance and receiving distance as short as possible.
9. Compute the scattering coefficient with online tools, estimate the received light intensity from 1 LED set as $I_0^{(1)}$.
10. Set $F_\sigma = 0.7$ as the basic loss-of-correlation, get $SNR = 1.5$, compute the σ_A with σ_n
11. Compute the light intensity I_c , and the LEDs amount by $I_c/I_c^{(1)}$

Following the computation process, all the components and parameters are settled from the interested volume and the interested characteristic structure scale.

3 Experimental computation in a jet flow example

In this section, we demonstrated the computation process of the visibility problem in a jet flow with approximate $15 \mu\text{m}$ diameter air-filled bubbles in a volume of $30 \text{ cm} \times 30 \text{ cm} \times 8 \text{ cm}$. The whole estimation are computed under the condition of International Standard Atmosphere (ISA).

3.1 Axisymmetric jet flow

The axisymmetric jet flow is one of the best canonical flow for understanding the turbulence. It has been interrogated using both experimental and theoretical methods. Based on the experimental investigation result by Hussein, Capp and George in 1993 [17], we model the jet velocity field in the same data model.

$$\frac{U_0}{U_c} = \frac{1}{B_u} \left(\frac{x}{D} - \frac{x_0}{D} \right), \quad (3.1)$$

where the U_0 is the jet exit velocity, U_c is the centreline velocity at position x , x_0 is the virtual origin of the jet, and D is the jet nozzle diameter.

According to the non-dimensionalized Reynolds stresses by the square of the centreline velocity in [17], the averaged fluctuation velocity can be computed from:

$$\frac{\overline{u^2}}{U_c^2} = 0.078 \quad (3.2)$$

According to measurement result in Preben Buchhave and Clara M. Velte in 2017[12], the length Taylor microscales are 2.2 mm and the temporal Taylor microscales are $1 \mu\text{s}$ at the center line at 30 D downstream location, which requires particle cut-off frequency higher than 1 kHz and camera repetition rate higher than 2 kHz. From 13mm radial distance off the jet centerline, the temporal Taylor microscales are $2 \mu\text{s}$, which requires particle cut-off frequency 500 Hz.

3.2 Seeding computation

The seeding tracers that we use to verify the method are the air-filled micron-scale bubble tracers, which have mean diameters of approximately $15\ \mu\text{m}$. Diogo C. Barros etc.[1] investigated the characteristics of the seeding in a wind tunnel experiment. The theoretical response time computed from equation (2.3) is $20\ \mu\text{s}$, and the measured mean response time was $40\ \mu\text{s}$. More details of the microbubble tracer and the bubble generator can be found in [1]

The reason we choose this type of seeding is that the tracers size is big enough to reflect light signal, and is small enough to show trajectory of Taylor microscale, and the response time is small enough to follow Taylor micro-scale. As the temporal Taylor micro-scales is $1\ \mu\text{s}$ at the center line at 30D downstream location for 1cm jet at $Re = 19868$ [12], the Stokes number of the micro-bubbles was found to be 0.04, which is in the acceptable upper limit of 0.1 [46].

According to Kerho and Bragg [18] and Afanasyev et al. [19], the wall thickness of soap bubbles lies in the range $0.1 \sim 0.3\ \mu\text{m}$, the density of the bubbles is $20 \sim 70\ \text{kg} \cdot \text{m}^{-3}$ [1]. Taking the visible bubble diameter from $10 \sim 30\ \mu\text{m}$, which have the frequency domain Stoke number at 0.26 and 0.47, the cut-off frequencies varies from 752.2 Hz for large high density bubbles to 6.77 kHz for small low density bubbles. And the mean cut-off frequency is 2.21 kHz for $15\ \mu\text{m}$ particles with $0.2\ \mu\text{m}$ wall thickness. So in the radial range of 13 mm at 30D downstream, only minor parts of the tracers (2.5% computed from statistics in [1]), of which the diameter is larger than $30\ \mu\text{m}$ and the wall thickness is thicker than $0.3\ \mu\text{m}$, cannot represent the Taylor micro-scale in the 10 mm jet. Out the radial range of 13 mm at 30 D downstream, all the tracers follows the Taylor micro-scale eddies well. For the average diameter particles, the energy transfer function in equation (2.7) equals to 0.7088, which is in the efficient response range [0.5, 2].

3.3 Imaging computation

Considering the sensor size $27.6\ \text{mm} \times 26.3\ \text{mm}$ with resolution $2048 \times 1944\text{px}$ and pixel pitch $13.5\ \mu\text{m}$, the magnification is 0.0875. Only computing the aperture number with $\lambda = 625\ \text{nm}$ that is the highest quantum efficient point of the camera used in the Section 4.1.2, the aperture number 13 is as $\text{DOF}=8\text{cm}$. So the F-stop is set at 16 due to the discrete number. The particle image τ_p is 1.97. To avoid to interfere the flow, the lens and the jet nozzle are in the same plane parallel to the front plane of the investigated volume, thus the distance from the object geometrical center to the lens center d_o is 35 cm with the camera angle at 30° . So the focal length f is 28.16 mm. The 35 mm lens is adapted due to discrete product models.

3.4 Light budget computation

The emission spectra of a white light LED consists of a wide wavelength band from 440 – 760 nm. In order to simplify the estimation of the image signal, we consider the optical power as if it is emitted at the single wavelength $\lambda = 625\ \text{nm}$, i.e. the following computation is based on $\lambda = 625\ \text{nm}$ and corresponding photon energy of 3.2×10^{-19} Joules. At this wavelength the Mie parameters x_M equals

Table 1: The computation results

Steps in Sec.2.5	Designed Variables	Utilizing parameters from given condition	Result	Unit
1	volume		$30 \times 30 \times 8$	cm
	ℓ		2.2	mm
	τ_f		1	ms
	U		22.65	m/s
2	f_c		2	kHz
3	d_p		15	μm
	ρ_p		20-70	$\text{kg} \cdot \text{m}^{-3}$
	ε		0.26-0.47	-
	$ H_p(\varepsilon) ^2$		0.7088	-
4	M		0.0875	-
	d_o		35	cm
5	f_s		16	-
	τ_p		2	pixel
	f		35	mm
6	x_m		75.4	-
7	ϑ		75	$^\circ$
8	$I_0^{(1)}$		41.6	counts
9	σ_A		10.8	-
10	I_0		148	-
	$I_0/I_0^{(1)}$		3.5	-

75.4, which is in the range of geometrical optics approximate computation. At the scattering angle of 90° , the light brightness at the target is 10^6 lux per LED. The averaged Mie scattering coefficient is about $8.6 \times 10^{-12} \text{ m}^2$. The received light energy of the CMOS detector is 2.95×10^{-18} Joules. The quantum efficiency of the CMOS detector of the camera at this photon energy is 0.95.

Plugging these parameters into the aforementioned model for estimating, the signal from one particle gives 8.8 counts for one LED set. If a LED can be pivoted to the cameras for acquiring a better scattering angle like , for example, 75° , the received light energy would be 1.39×10^{-17} Joules, and the particle signal on the sensor is about 41.6 counts for each LED set. The noise level of the CMOS detector is $\sigma_n = 7.2$, the signal level is 10.8 and the required light density I_c is 148 counts with assuming $N_{ppp} = 0.01$. So the number of required LED sets is 3.5. Because all the computation are conserved, we choose to use 3 LEDs in the experiment.

3.5 Computation result

To summarize all the computation in this section, the steps and results are shown in the following table 1. Every step is computed base on the Section 2.5. As described from Section 3, all the variables are

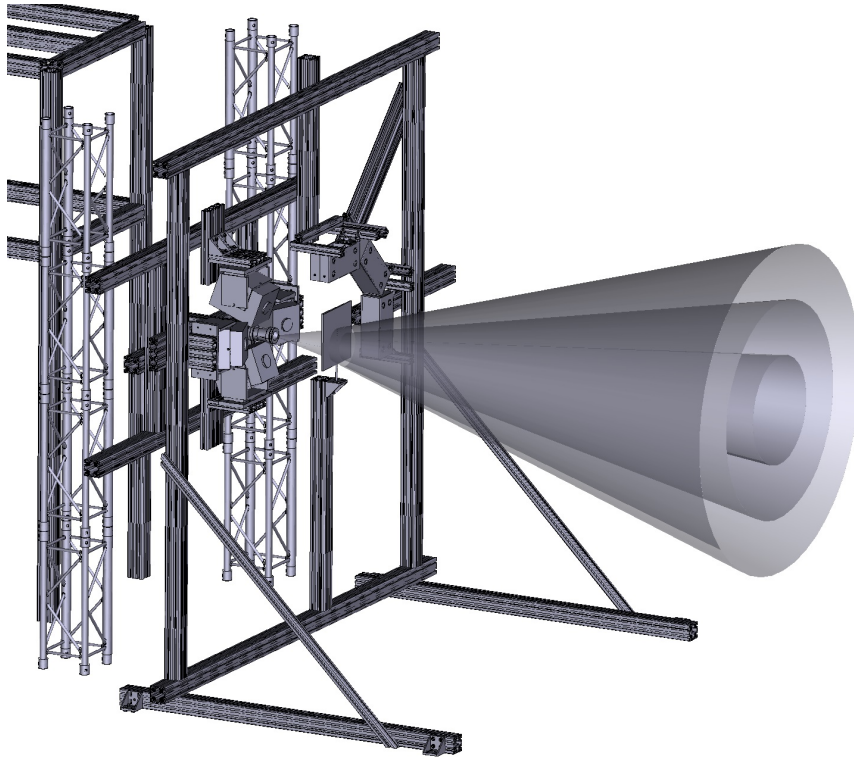


Figure 2: The Full Field section in Turbulence Research Laboratory at Technical University of Denmark

4 Experiment and results

Experiments are conducted in a jet flow facility of the Turbulence Research Laboratory (TRL) of the Department of Mechanical Engineering at Technical University of Denmark. The TRL consists of 2 test sections – the High resolution section and the Full Field section [2]. All the experiments in this paper are implemented in the Full Field section.

4.1 Experimental setup

4.1.1 Jet

In the Full Field test section, a jet with 10 mm diameter nozzle was placed in the center of injection wall. At the end of jet downstream direction, a sucking plate was mounted on the sucking wall. The whole Full Field Test Section have volume of 4480 mm(streamwise length) \times 4110 mm(width) \times 4930 mm(height). Outside of the test section, there is an air recirculation controlling the air flow and the seeding density without influencing flow in the test cell.

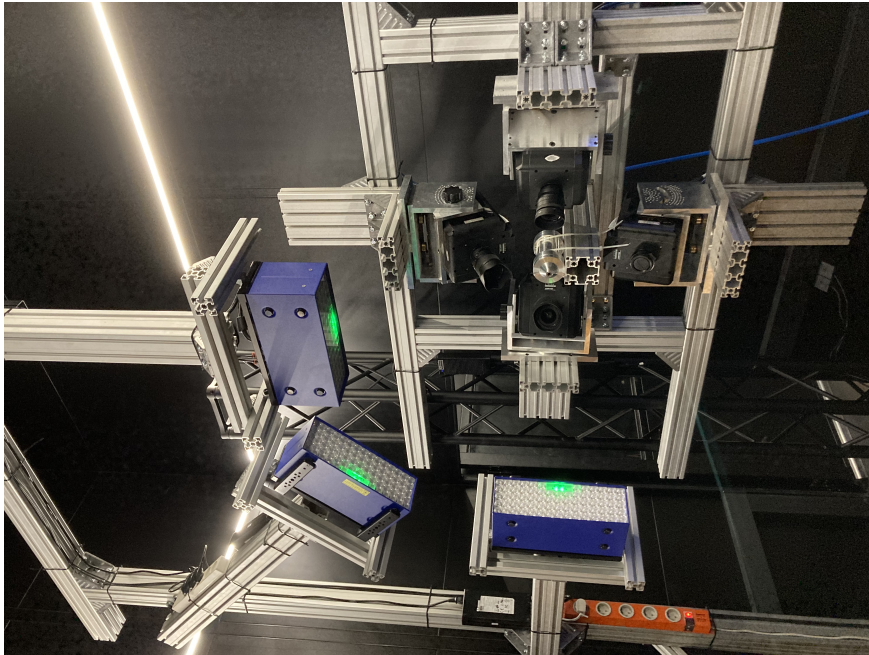


Figure 3: The setup for these two measurements.

4.1.2 Cameras

The visualization system that we used is a commercial LaVision PIV/PTV system, which consists of four 2048×1944 px CMOS high-speed video cameras (v2640), a Programmable Timing Unit (PTU) and system software Davis10. The sensor size is $27.6\text{mm} \times 26.3\text{mm}$, and the pixel pitch is $13.5\mu\text{m}$ with 12-bit depth. The cameras were arranged symmetrically facing the volume of interest (VOI), as shown in Figure 3.

The cameras were angled at $\alpha = 30^\circ$ to the jet center line. The cameras were mounted on a 4 degree of freedom frame, which help to adjust the view angle at the minimum point independently. According to computation from , the lens focal length is 35mm, and the aperture is set at f# 8.

4.1.3 Lights

The light sources we use in the experiment are an array of Flashlight 300 LEDs, which is produced by LaVision GmbH. These high power LEDs consist of 72 diodes each. The opening angle is 10° . In the pulsed-overdrive mode, the LEDs are operated above the nominal LED current to generate short pulses at about 5 times high light intensities than the free trigger mode. but to protect the LEDs at such high current, the duty cycle is limited to a maximum of 10%. The brightness can be measured above 10^6 lux at 1m distance.

In order to acquire better light single, forward scattering is applied by rotating the LEDs to the camera. The forward LED angles for each camera are measured and demonstrated in the Table 2

Table 2: The angle from LEDs to cameras

Camera	LED1	LED2	LED3
Camera no.1	120	120	120
Camera no.2	130	130	130
Camera no.3	140	140	140
Camera no.4	150	150	150

4.2 Seeding

The air-filled soap bubble generator used in this paper was developed by TSI and had been applied for several wind tunnel experiments. It consists of a 57L reservoir filled with a 5% surfactant-water solution. The surfactant was common non-color and non-perfume pure dish-washing detergent. At bottom of the reservoir, a piston pump is used to draw and pressurize the solution through a high pressure tube with a set of 10 nozzles. The outlet diameter of the nozzles is 0.2mm, and could be blocked with special blank nozzle heads to reduce the seeding generating rate.

The air-filled-soap-bubble tracers have mean diameter of $14.7 \mu\text{m}$, response time $40 \mu\text{s}$ with a dispersion of $30 \mu\text{m}$. The bubbles can be generated at high rates of 50 tracers per cm^3 . The Stokes number of the micro-bubbles was 0.04, which could show the flow trajectory faithfully[13].

4.2.1 Shadowgraph results of $15 \mu\text{m}$ bubbles

4.2.2 Phase Doppler Anemometry results of $15 \mu\text{m}$ bubbles

4.3 Experiment process

The demonstrated volumetric measurements of 4D PTV are implemented into two tests in a 10 mm round jet. The first test is carried out at $Re = 2 \times 10^4$ within a domain from 30D to 38D 2930cm^3 , which lies between the traditional volumetric domains investigated using either DEHS droplets or HSFB bubbles. The second test Reynolds number is 25,000, and the domain starts from 70D to 78D, which equals to the same volumetric domain that are presented in.

The data analysis is performed with LaVision software Davis 10.3. For post-processing, the images were processed using the following steps to reduce noise: 1) apply a 3×3 pixel Gaussian filter to remove the noise; 2) subtract a local median (9×9 pixels) to remove the background; 3) subtract a constant intensity of 10 and multiply by a constant value of 5 to increase the contrast; 4) apply a 7×7 pixel Gaussian filter to facilitate the particle identification process.

4.4 Experimental Results

4.4.1 Light signal result

For each snapshot, the number of the traced particles was in the range $7 \times 10^4 \sim 9 \times 10^4$. The signal-to-noise ratio (SNR) of the raw images is 1.6, which is higher than the estimated 1.5. This may be due to the inhomogeneous plane light that increases forward scattering, and high density of bubbles that may

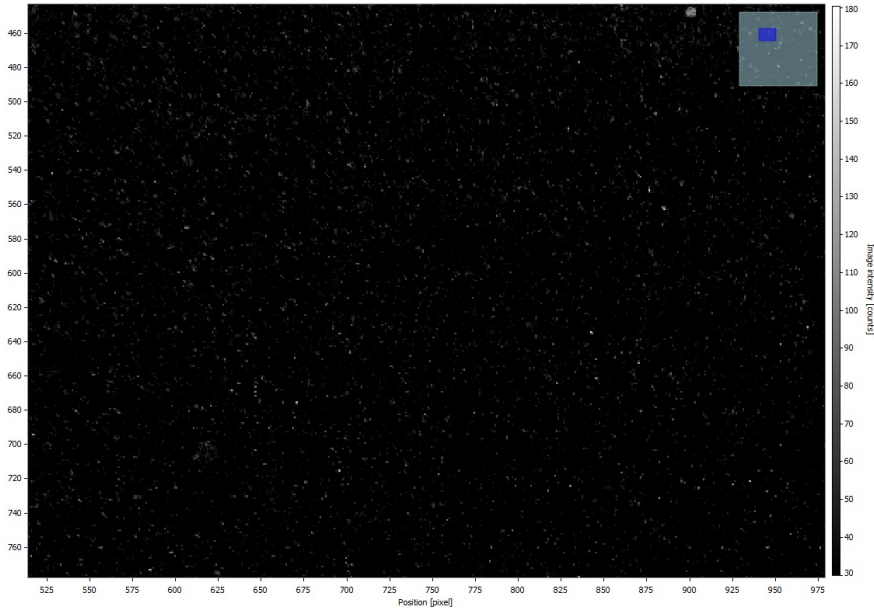


Figure 4: The sub-image of the measurement.

also contribute to the scattering light intensity [20].

A sample image acquired by one camera was shown in Fig. 4, in which the particles can be clearly identified by the LaVision Davis system. The averaged size of particle image is 4 pixels in agreement with computation, and the signal from the camera sensor is about 80-160 counts, which is in the same level with the estimated 147 counts in section 3. The main difference may be due to the different angle of LED to different cameras.

4.4.2 Reconstructed result

4.4.3 Global structure and Taylor micro-scale structure

5 Conclusion and discussion

To cover the whole range from the global eddies to the smallest interested eddies, the relations of particle size, imaging, light intensity are formulated. From the characteristic timescale and length scale of the smallest interested eddies, the tracer type can be chosen by the diameter and density. Then the light intensity can be estimated from the particle and the necessary minimum distance of the setup. With all the computed parameters, one setup for jet flow measurement was prepared for the volumetric velocimetry in the volume of $\geq 2 \times 10^3 \text{ cm}^3$ and $\geq 9 \times 10^3 \text{ cm}^3$. The selected seeding tracer is air-filled soap bubbles with diameter of approximately $15 \mu\text{m}$, of which the size of seeding tracer is between millimeter scale HFSB and $1 \mu\text{m}$ scale DEHS. The targeted measurement volume dimension is equivalent to the volume of HFSB, which will give a higher resolution of turbulence study.

The evaluation method in Section 2 can successfully predict the visibility of the

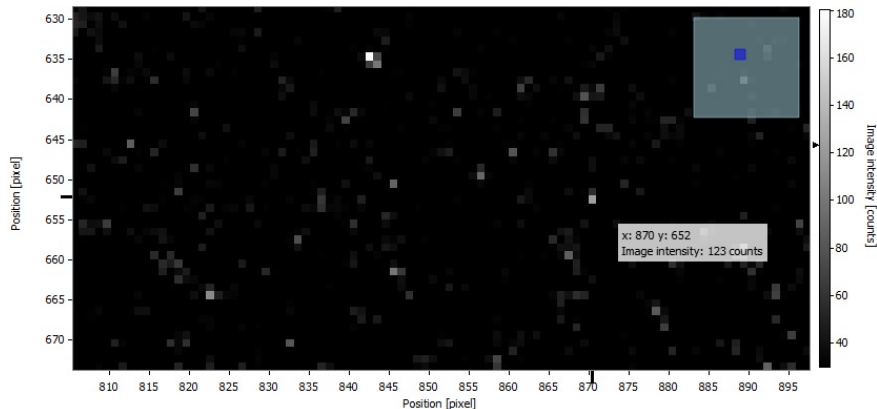


Figure 5: The signal intensity is 80-160 counts.

small tracers. The Taylor micro-scale can be observed in the same time to catch the global eddies at $Re = 2 \times 10^4$ in the 10 mm jet flow. A higher Reynolds number is possible to be achieved with well designed illumination source. Also a full field volumetric velocimetry of a jet flow from 30D to 100D can be implemented with more cameras due to the limited DOF of each lens. Further developments aim to reach higher Reynolds number and larger DOF.

Before the experiment designs, it is better to define an index of light cost per signal counts that could help to evaluate the illumination options under the limited budget. In a larger volumes, the low cost LED lights, which pave for the basic light intensity to the threshold with the problem of illuminating unnecessary volume, can be adapted to accompany the high cost high-power laser with mirrors reflection, which increase the critical signals within the limited volume. Because the LED lights are highly limited by the distance due to the open angle, and the laser are highly limited by the reflection times due to energy loss in each reflection.

Our further work is to observe Taylor micro-scale in the same time to catch the global eddies at $Re = 2 \times 10^4$ in the 1 cm jet flow. A higher Reynolds number is possible to be achieved with well designed illumination source.

6 Acknowledgements

Yisheng Zhang, Simon L. Ribergård and Clara M. Velte acknowledge financial support from the European Research council: This project has received funding from the European Research Council (ERC) under the European Unions Horizon 2020 research and innovation program (grant agreement No 803419).

Haim Abitan acknowledges financial support from the Poul Due Jensen Foundation: Financial support from the Poul Due Jensen Foundation (Grundfos Foundation) for this research is gratefully acknowledged.

We all also acknowledge Knud Erik Meyer and Niels S. Jensen for his help in our experimental implement.

The Department of Mechanical Engineering at the Technical University of Denmark is also acknowledged for their generous additional support in establishing the laboratory.

7 Bibliography

- [1] Diogo C. Barros, Yanchong Duan, Daniel R. Troolin, Ellen K. Longmire, Air-filled soap bubbles for volumetric velocity measurements, *Experiments in Fluids*, 62, 36 (2021)
- [2] S.L. Ribergaard, Y. Zhang, H. Abitan, J.S. Nielsen, N.S. Jensen, C.M. Velte, A novel laboratory pushing the limits for optics-based basic turbulence investigations, 14th International Symposium on Particle Image Velocimetry – ISPIV 2021, August 1–5, 2021
- [3] Michaelis D, Bompfrey R, Henningsson P, Hollis D, Reconstructing the vortex skeleton of the desert locust using phase averaged POD approximations from time resolved thin volume tomographic PIV. In: 16th International symposium on applications of laser techniques to fluid mechanics, Lisbon, Portugal (2012)
- [4] Elsinga GE, Scarano F, Wieneke B, van Oudheusden BW, Tomographic particle image velocimetry. *Experiments in Fluids*, 41(6),933–947 (2006)
- [5] Discetti S, Coletti F, Volumetric, velocimetry for fluid flows. *Meas Sci Technol*, 29(4):042,001(2018)
- [6] Scarano F., Ghaemi S., Caridi G.C.A., Bosbach J., Dierksheide U., Sciacchitano A., On the use of helium-filled soap bubbles for large-scale tomographic PIV in wind tunnel experiments. *Experiments in Fluids*, 56:42,(2015)
- [7] Schröder A, Geisler R, Sieverling A, Wieneke B, Henning A, Scarano F, Elsinga GE, Poelma C, Lagrangian aspects of coherent structures in a turbulent boundary layer flow using TR-Tomo PIV and FTV, 8th international symposium on particle image velocimetry, ,(2009)
- [8] Humble R, Elsinga G, Scarano F, Van Oudheusden B, Three dimensional instantaneous structure of a shock wave/turbulent boundary layer interaction. *Journal of Fluid Mechanics*, 622, 33–62 (2009)
- [9] Violato D, Moore P, Scarano F, Lagrangian and Eulerian pressure field evaluation of rod-airfoil flow from time-resolved tomographic PIV. *Experiments in Fluids*, 50(4),1057–1070(2011)
- [10] Ghaemi S, Scarano F, Counter-hairpin vortices in the turbulent wake of a sharp trailing edge. *Journal of Fluid Mechanics*, 689, 317–356(2011)
- [11] Schröder A, Geisler R, Staack K, Elsinga GE, Scarano F, Wieneke B, Westerweel J. Eulerian and Lagrangian views of a turbulent boundary layer flow using time-resolved tomographic PIV. *Experiments in Fluids*, 50, 1071–1091 (2011)
- [12] Preben Buchhave and Clara M. Velte, Measurement of turbulent spatial structure and kinetic energy spectrum by exact temporal-to-spatial mapping, *Phys.Fluids*, 29, 085109 (2017)
- [13] Voth G., LA Porta A., Crawford A., Alexander J., Bodenschatz E., Measurement of particle accelerations in fully developed turbulence. *Journal of Fluid Mechanics*, 469, 121-160 (2002)

- [14] Atkinson C, Coudert S, Foucaut JM, Stanislas M, Soria J, The accuracy of tomographic particle image velocimetry for measurements of a turbulent boundary layer. *Experiments in Fluids*, 50(4), 1031–1056(2011)
- [15] Kühn M, Ehrenfried K, Bosbach J, Wagner C, Large-scale tomographic particle image velocimetry using helium-filled soap bubbles. *Experiments in Fluids*, 50(4), 929–948 (2011)
- [16] Mei R, Velocity fidelity of flow tracer particles. *Experiments in Fluids*, 22(1), 1-13(1996)
- [17] Hussein H., Capp S., George W., Velocity measurements in a high-Reynolds-number, momentum-conserving, axisymmetric, turbulent jet. *Journal of Fluid Mechanics*, 258, 31-75 (1994)
- [18] Kerho MF, Bragg MB, Neutrally buoyant bubbles used as flow tracers in air. *Experiments in Fluids*, 16(6),393–400 (1994)
- [19] Afanasyev Y, Andrews G, Deacon C., Measuring soap bubble thickness with color matching. *American Journal of Physics*, 79(10), 1079–1082(2011)
- [20] Scharnowski S, Kahler CJ, On the loss-of-correlation due to PIV image noise. *Experiments in Fluids*, 57,119 (2016)
- [21] Gioacchino Cafiero, Stefano Discetti, Tommaso Astarita, Flow field topology of submerged jets with fractal generated turbulence. *Physics of Fluids* 27, 115103 (2015)
- [22] Caridi, G.C.A., Ragni, D., Sciacchitano, A. et al., HFSB-seeding for large-scale tomographic PIV in wind tunnels. *Experiments in Fluids*, 57, 190 (2016).
- [23] Toufik Boushaki, Amine Koched, Zakaria Mansouri, Florian Lespinasse, Volumetric velocity measurements (V3V) on turbulent swirling flows. *Flow Measurement and Instrumentation*, 54, 46-55(2017)
- [24] Pröbsting, S., Scarano, F., Bernardini, M. et al., On the estimation of wall pressure coherence using time-resolved tomographic PIV. *Experiments in Fluids*, 54, 1567 (2013).
- [25] Schneiders JF, Caridi GC, Sciacchitano A, Scarano F, Largescale volumetric pressure from tomographic PTV with HFSB tracers. *Experiments in Fluids*, 57(11):164 (2016)
- [26] Schneiders JF, Scarano F, Dense velocity reconstruction from tomographic PTV with material derivatives. *Experiments in Fluids*, 57(9):139(2016)
- [27] Schröder A, Geisler R, Elsinga GE, Scarano F, Dierksheide U, Investigation of a turbulent spot and a tripped turbulent boundary layer flow using time-resolved tomographic PIV. *Experiments in Fluids*, 44(2):305–316(2007)
- [28] Terra W, Sciacchitano A, Scarano F, Aerodynamic drag of a transiting sphere by large-scale tomographic-PIV. *Experiments in Fluids*, 58(7):83(2017)
- [29] Jianfeng Hou, Frieder Kaiser, Andrea Sciacchitano, David E. Rival, A novel single-camera approach to large-scale, three-dimensional particle tracking based on glare-point spacing. *Experiments in Fluids*, 62:100(2021)

- [30] Johannes Bosbach, Matthias Kühn, Claus Wagner, Large scale particle image velocimetry with helium filled soap bubbles. *Experiments in Fluids*, 46, pages 539–547 (2009)
- [31] Jan F. G. Schneiders, Giuseppe C. A. Caridi, Andrea Sciacchitano, Fulvio Scarano, Large-scale volumetric pressure from tomographic PTV with HFSB tracers. *Experiments in Fluids*, 57(11) (2016)
- [32] Florian Huhn, Daniel Schanz, Sebastian Gesemann, Uwe Dierksheide, Remco van de Meerendonk, Andreas Schröder, Large-scale volumetric flow measurement in a pure thermal plume by dense tracking of helium-filled soap bubbles. *Experiments in Fluids*, 58:116 (2017)
- [33] Schanz Daniel, Geisler R., Voss C., Novara M., Jahn T., Dierksheide U., Schröder A., Large scale volumetric flow measurements in a turbulent boundary layer. 8th International Symposium on Flow Visualization, Zurich, Switzerland, June 26-29, 2018
- [34] Johannes Bosbach, Daniel Schanz, Philipp Godbersen, Andreas Schröder, Dense Lagrangian particle tracking of turbulent Rayleigh Bénard convection in a cylindrical sample using Shake-The-Box. 17th European turbulence conference, 3-6 September 2019, Torino Italy
- [35] Daniel Schanz, Matteo Novara, Reinhard Geisler, Janos Agocs, Felix Eich, Matthew Bross, Christian J. Kähler, Andreas Schröder, Large-scale volumetric characterization of a turbulent boundary layer flow. 13th International Symposium on Particle Image Velocimetry – ISPIV, Munich, Germany, July 22-24, 2019
- [36] Daniel Schanz, Florian Huhn, Sebastian Gesemann, Uwe Dierksheide, Remco van de Meerendonk, Peter Manovski, Andreas Schröder, Towards high-resolution 3D flow field measurements at cubic meter scales. 18th International Symposium on the Application of Laser and Imaging Techniques to Fluid Mechanics, Lisbon, Portugal, 4–7 July, 2016
- [37] C. Christian Wolf, Clemens Schwarz, Kurt Kaufmann, Anthony D. Gardner, Dirk Michaelis, Johannes Bosbach, Daniel Schanz, Andreas Schröder, Experimental study of secondary vortex structures in a rotor wake. *Experiments in Fluids*, 60:175(2019)
- [38] M. Novara, D. Schanz, R. Geisler, J. Agocs¹, F. Eich, M. Bross, C. J. Kähler, A. Schröder, Investigation of turbulent boundary layer flows with adverse pressure gradient by means of 3D Lagrangian particle tracking with Shake-The-Box. 14th International Symposium on Particle Image Velocimetry – ISPIV 2021, August 1–5, 2021
- [39] F. Huhn, D. Schanz, P. Manovski, S. Gesemann, A. Schröder, Time-resolved large-scale volumetric pressure fields of an impinging jet from dense Lagrangian particle tracking. *Experiments in Fluids*, 59:81 (2018)
- [40] J. Bosbach, D. Schanz, P. Godbersen, A. Schröder, Spatially and Temporally Resolved Measurements of Turbulent Rayleigh-Bénard Convection by Lagrangian Particle Tracking of Long-Lived Helium-Filled Soap Bubbles. 14th

International Symposium on Particle Image Velocimetry – ISPIV 2021, August 1–5, 2021

- [41] A. Schröder, D. Schanz, J. Bosbach, M. Novara, R. Geisler, J. Agocs, A. Kohl, Large-scale 3D flow investigations around a cyclically breathing thermal manikin in a 12 m³ room using HFSB and STB. 14th International Symposium on Particle Image Velocimetry – ISPIV 2021, August 1–5, 2021
- [42] Lobutova E, Resagk C, Rank R, Müller D, Extended three dimensional particle tracking velocimetry for large enclosures. In Imaging measurement methods for flow analysis, Springer, Berlin, 113–124 (2009)
- [43] Stephen B. Pope, Turbulent Flows. Cambridge University Press, Cambridge(UK), 183–185 (2000)
- [44] Ronald J. Adrian, Jerry Westerweel, Particle Image Velocimetry. Cambridge University Press, Cambridge(UK), 183–185 (2011)
- [45] Raffel, M., Willert, C.E., Scarano, F., Kähler, C., Wereley, S.T., Kompenhans, J., Particle Image Velocimetry: A Practical Guide Third Edition. Springer International Publishing, 33–35 (2018)
- [46] Tropea C., Foss J.F., Yarin A., Springer Handbook of Experimental Fluid Mechanics. Springer, Berlin, Heidelberg, 287–289 (2007)
- [47] van de Hulst H.C., Light scattering by small particles. Dover Publications, Toronto, Canada, 200–227 (1981)
- [48] Bohren C.F., Huffman D.R., Absorption and Scattering of Light by Small Particles. A Wiley-Interscience Publication, Toronto, Canada, 83–129 (1983)
- [49] Mishchenko M.I., Travis L.D., Lacis A.A., Scattering, absorption, and emission of light by small particles. Cambridge University Press, Cambridge, UK, 115–190 (2002)
- [50] Born M., Wolf E., Principles of Optics (60th anniversary edition). Cambridge University Press, Cambridge, UK, 735–785 (2019)